

Elucidating the Mechanism of Li Insertion into $\text{Fe}_{1-x}\text{S}/\text{Carbon}$ via *In Operando* Synchrotron Studies

Chengping Li, Angelina Sarapulova, Kristina Pfeifer, Xianlin Luo, Nicola Pietro Maria Casati, Edmund Welter, Georgian Melinte, Qiang Fu, and Sonia Dsoke*



Cite This: *ACS Appl. Mater. Interfaces* 2020, 12, 52691–52700



Read Online

ACCESS |



Metrics & More



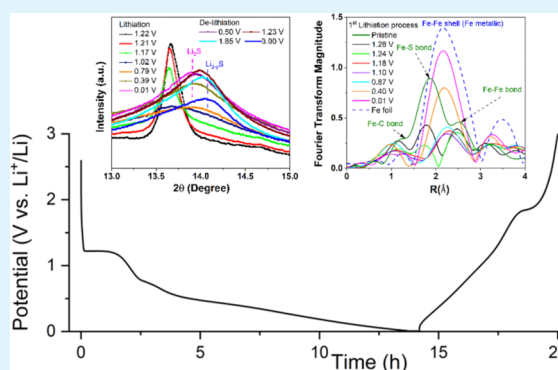
Article Recommendations



Supporting Information

ABSTRACT: The detailed understanding of kinetic and phase dynamics taking place in lithium-ion batteries (LIBs) is crucial for optimizing their properties. It was previously reported that $\text{Fe}_{1-x}\text{S}/\text{C}$ nanocomposites display a superior performance as anode materials in LIBs. However, the underlying lithium storage mechanism was not entirely understood during the 1st cycle. In this work, *in operando* synchrotron techniques are used to track lithium storage mechanisms during the 1st (de)-lithiation process in the $\text{Fe}_{1-x}\text{S}/\text{C}$ nanocomposite. The combination of *in operando* techniques enables the uncovering of the phase fraction alternations and crystal structural variations on different length-scales. Additionally, the investigation of kinetic processes, morphological changes, and internal resistance dynamics is discussed. These results reveal that the phase transition of $\text{Fe}_{1-x}\text{S} \rightarrow \text{Li}_2\text{Fe}_{1-x}\text{S}_2 \rightarrow \text{Fe}^0 + \text{Li}_2\text{S}$ occurs during the 1st lithiation process. The redox reaction of $\text{Fe}^{2+} + 2\text{e}^- \rightleftharpoons \text{Fe}^0$ and the Fe K-edge X-ray absorption spectroscopy (XAS) transformation process are confirmed by *in operando* XAS. During the 1st de-lithiation process, Fe^0 and Li_2S convert to $\text{Li}_{2-y}\text{Fe}_{1-x}\text{S}_2$ and Li^+ is extracted from Li_2S to form Li_{2-y}S . The phase transition from Li_2S to Li_{2-y}S is not detected in previous reports. After the 1st de-lithiation process, amorphous lithiated iron sulfide nanoparticles are embedded within the remaining Li_2S matrix.

KEYWORDS: *in operando* synchrotron X-ray diffraction, lithium storage mechanism, conversion reaction, X-ray absorption spectroscopy, phase transition



1. INTRODUCTION

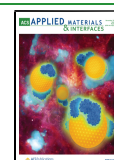
To meet the ever-rising demands of durable, high energy density secondary batteries, many strategies are dedicated to optimize electrode materials' properties of lithium-ion batteries (LIBs).^{1–3} Metal sulfides (CoS_2 , SnS_2 , FeS , Sb_3S_4 , MoS_2 , etc.) attracted attention because of their high specific capacity, low cost, and natural abundance.^{4–7} Among them, FeS-based electrode materials have advantages such as a high theoretical capacity of 609 mA h g^{-1} and abundant resources.⁸ However, a FeS-based anode material suffers from rapid capacity fading and is caused by the huge volume expansion and the severe side reactions during electrochemical reactions. More deleteriously, the formation of the insulating polysulfide Li_2S_x ($2 < x < 8$) impairs further electrochemical reactions.^{9,10} Owing to these shortcomings, at the present state of technology, such types of conversion-type materials cannot be used for real applications, but research on the elucidation of the Li^+ -ion insertion/extraction mechanism and optimization of the properties is crucial to make these materials more promising. According to previous reports, the theoretical volume changes of the FeS electrode can reach 200% during continuous lithiation and de-lithiation processes.¹¹ Additionally, the low

electronic conductivity of FeS-based materials negatively hinders Li^+ -ion transfer, leading to an inferior electrochemical performance. To solve these issues, some solutions, such as downsizing the metal sulfide particles and combining them with elastic and conductive carbonaceous materials, have been explored.^{12,13} Metal sulfide particles with nanometer-scale significantly improve the reaction efficiency and alleviate the structural strain during the electrochemical process.¹⁴ A carbon matrix can support the host materials by improving the electronic conductivity and buffering volume changes.^{15–18} These strategies are appealing approaches to enhance the rate performance and cycling stability. A deep study of Li^+ -ion storage mechanism and electrochemical performance is vital to further practical applications. However, the mechanism of lithium storage into FeS-based electrode materials during

Received: August 28, 2020

Accepted: November 4, 2020

Published: November 16, 2020



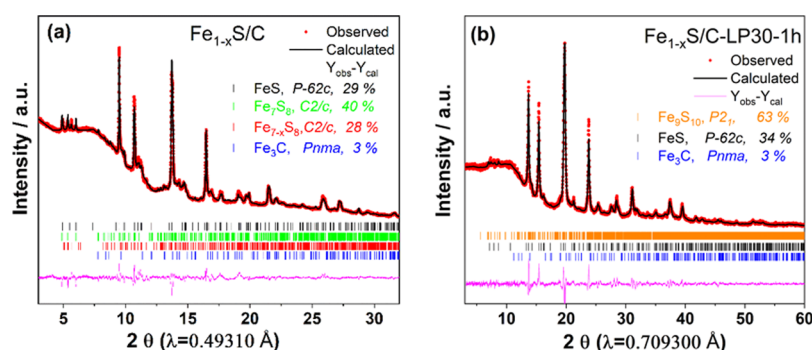


Figure 1. X-ray radiation diffraction of the pristine $\text{Fe}_{1-x}\text{S}/\text{C}$ (a) and the pristine $\text{Fe}_{1-x}\text{S}/\text{C}$ material in the LP30 electrolyte for 1 h (b).

lithiation and de-lithiation processes is still under debate. McMillan et al. claimed that the intermediate Li_2FeS_2 does not exist by using Fe Mössbauer spectroscopy.¹⁹ Some previous research works reported that the reduction of Fe_{1-x}S forms the intermediate product of Li_2FeS_2 .^{20–22} However, there is no evidence that the intermediate Li_2FeS_2 is existing. Therefore, a fundamental question remains: what is the product of the conversion of a FeS-based material during the first lithiation and de-lithiation processes? Furthermore, according to the state-of-the-art literature, there is a lack of reports about the structural evolution and tracking of the local environment changes by using X-ray absorption spectroscopy (XAS) for the FeS-based electrode.

The purpose of this work is to answer these unsolved questions. This study focuses on the fundamental understanding of the crystalline structure changes by observing phase transitions based on *in operando* synchrotron radiation diffraction. Meanwhile, this work aims to track the changes of the local environment and electronic transitions at the Fe K-edge XAS through *in operando* XAS during the 1st lithiation process. The surface morphology variation of the cycled electrodes is observed by *ex situ* scanning electron microscopy (*ex situ* SEM). Electrochemical impedance spectroscopy (EIS) is used to investigate the charge-transfer resistance and solid electrochemical interphase resistance of the $\text{Fe}_{1-x}\text{S}/\text{C}$ electrode during the 1st lithiation/de-lithiation processes.

2. RESULTS AND DISCUSSION

2.1. Structural and Morphological Characterization.

Figure 1a shows the crystal structure of the pristine $\text{Fe}_{1-x}\text{S}/\text{C}$ material. The Rietveld refinement demonstrates that the pristine $\text{Fe}_{1-x}\text{S}/\text{C}$ material consists of a FeS phase, two phases of Fe_7S_8 , and a Fe_3C phase. In detail, the FeS phase (29%) has a space group of $P\bar{6}2c$; the Fe_7S_8 phase has a space group of $C2/c$, with part stoichiometric (40%) and nonstoichiometric (28%); and the Fe_3C phase (3%) has a space group of $Pnma$. The pristine material is labeled $\text{Fe}_{1-x}\text{S}/\text{C}$ for simplicity. The x in $\text{Fe}_{1-x}\text{S}/\text{C}$ ($0 \leq x \leq 0.125$) varies from 0 (the FeS phase, 29%, space group of $P\bar{6}2c$) to 0.125 [the Fe_7S_8 phase, stoichiometric (40%) and nonstoichiometric (28%), space group of $C2/c$]. The composition of $\text{Fe}_{1-x}\text{S}/\text{C}$ is nonstoichiometric because of ordered vacancies inside the Fe lattice.^{23–25} The presence of the Fe_3C phase is beneficial for the capacity increase, as already highlighted in our previous work.²⁶ Many strategies have been used to prepare a single-phase iron sulfide material for exploring the lithium storage mechanism.^{23–25} However unfortunately, the obtained sample always contains multiphases. There are some challenges to

prepare single-phase iron sulfide compared with iron oxides, which are summarized as follows: (1) iron sulfides have a complicated stoichiometry because of the instability of ferric ions and sulfide ions; (2) ferric ions can easily combine with oxygen, and the obtained products could contain iron oxide or iron hydroxide impurities; and (3) the phase diagram of iron sulfides is very complicated. FeS is formed at high reaction temperature (320 °C) and Fe_7S_8 formation appears at low reaction temperature (260 °C).²⁵

The pristine material was immersed in the LP30 commercial electrolyte for 1 h to observe the effect of the pristine $\text{Fe}_{1-x}\text{S}/\text{C}$ contact with the LP30 commercial electrolyte. No optical changes in the material or the electrolyte were observed. Nevertheless, for the investigation of nonvisible spontaneous processes, the resulting structural changes of $\text{Fe}_{1-x}\text{S}/\text{C}$ are analyzed (Figure 1b) and compared to the pristine material (Figure 1a). The phase fraction of $\text{Fe}_{1-x}\text{S}/\text{C}$ changes after immersion in LP30. The Fe_9S_{10} ($P2_1$, 63%) and FeS ($P\bar{6}2c$, 34%) phases are confirmed from the Rietveld refinement. The iron sulfide group consists of troilite (FeS) and pyrrhotites with continuously variable compositions. In detail, Fe_7S_8 (4C) has a monoclinic structure with a magnetic property; other pyrrhotites [Fe_9S_{10} (5C) and $\text{Fe}_{11}\text{S}_{12}$ (6C)] have a hexagonal structure with a nonmagnetic property.^{27–29} Fe_7S_8 (4C) is recognized as charge-neutral when written as $\text{Fe}_2^{3+}\text{Fe}_5^{2+}\text{S}_8$, which has 29% of Fe^{3+} . In comparison, Fe_9S_{10} (5C) is written as $\text{Fe}_2^{3+}\text{Fe}_7^{2+}\text{S}_{10}$, which contains 22% of Fe^{3+} . Additionally, according to literature reports,^{27,30} Fe_7S_8 (4C) has 12.5% of vacancies and Fe_9S_{10} (5C) has less vacancies (10%). The different amounts of Fe^{3+} and vacancies of pyrrhotites coexist in the pristine $\text{Fe}_{1-x}\text{S}/\text{C}$. The electrolyte (LP30) could stimulate the phase transition from Fe_7S_8 (4C) to Fe_9S_{10} (5C).

The composition of the Fe_{1-x}S material strongly depends on the synthesis conditions. The high-temperature treatment initiates the phase transition into pyrrhotite. It is not excluded that part of the material can also be present in the amorphous state. In our synthesized material, most of the mass belongs to the Fe_7S_8 composition. The electrolyte medium provides Li^+ ions, which can be absorbed by the material *via* diffusion on the Fe_7S_8 surface. Finally, the phase transition can be shifted as $\text{Fe}_7\text{S}_8 \rightarrow \text{Fe}_9\text{S}_{10}$ to compensate overcharge with Li^+ ions on the surface. This process is opposite to the pyritization process, described in ref 31. For a more detailed phase transition mechanism, more advanced characterization techniques [X-ray photoelectron spectroscopy (XPS), transmission electron microscopy (TEM), and SEM/EDX] are required. Haines *et al.* group theoretically investigated the structural instability between troilite (FeS) and pyrrhotite (Fe_{1-x}S). They found

that Fe_7S_8 (4C) and Fe_9S_{10} (5C) phases coexist at room temperature and easily transform into each other.³² In the following electrochemical characterization part of this paper, the active material is labeled as $\text{Fe}_{1-x}\text{S}/\text{C-LP30-1h}$ (which contains Fe_9S_{10} and FeS phases). Table S1 and S2 display the detailed information about the cell parameters and the Rietveld refinements (χ^2 , R_p , R_{wp} , etc.) of each phase.

As observed from SEM images in Figure 2a, the pristine $\text{Fe}_{1-x}\text{S}/\text{C}$ has Fe_{1-x}S nanoparticles (50–60 nm), which are

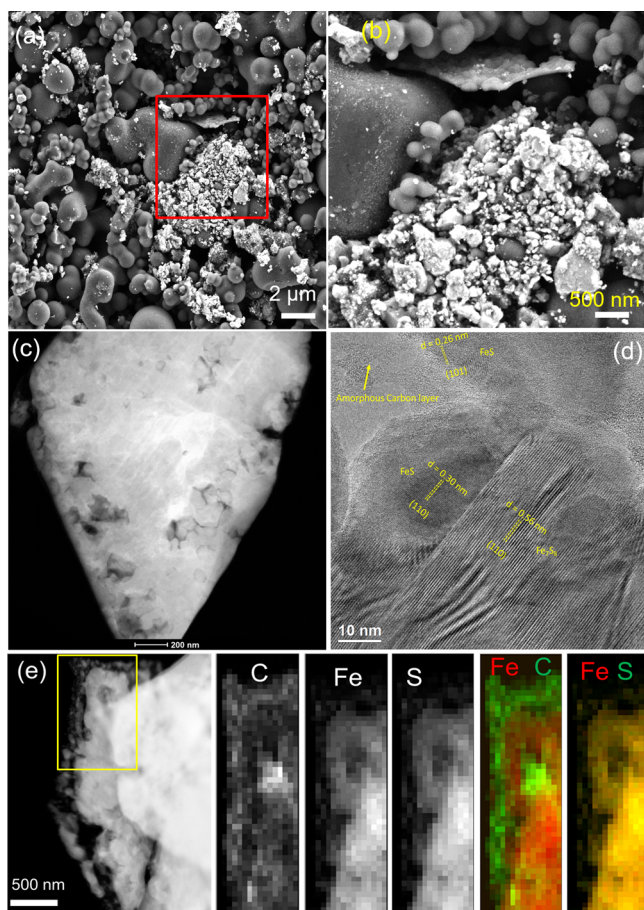


Figure 2. (a) SEM image and (b) high-magnification SEM image; (c) STEM and (d) HR-TEM image; and (e) STEM–EDS of the pristine $\text{Fe}_{1-x}\text{S}/\text{C}$ material.

surrounded by interconnected carbon microspheres (1–2 μm). Additionally, the $\text{Fe}_{1-x}\text{S}/\text{C}$ composite also has several forms of carbon. Among them, the amorphous carbon covers all particles and provides interconnection in the system. This unique Fe_{1-x}S nanoparticle-carbon microsphere structure has significant impacts on the cycling stability of the $\text{Fe}_{1-x}\text{S}/\text{C}$ electrode. The interconnected carbon microspheres enhance the electron conductivity and maintain a structural integrity. Furthermore, the space located between the Fe_{1-x}S active material and carbon microspheres alleviates the mechanical stress during the electrochemical reaction.²⁶ Therefore, the inhomogeneity distribution of carbon microspheres and Fe_{1-x}S nanoparticles is beneficial for the capacity retention and structural stability of the $\text{Fe}_{1-x}\text{S}/\text{C}$ electrode. The energy-dispersive X-ray spectroscopy (EDS) confirms that Fe and S are homogeneously distributed and surrounded by C in the as-prepared product (Figure S1a–d). Furthermore, the scanning transmission electron microscopy (STEM) imaging demonstrates that Fe_{1-x}S nanoparticles have an irregular shape (1–2 μm) composed of nanocomposites (50 nm) in Figure 2c. The high-resolution TEM (HR-TEM) imaging (Figure 2d) reveals a polycrystalline sample composed of interconnected nanograins with different crystalline orientations. Figure 2d shows a lattice spacing of 0.56 nm, which is related to the (110) plane of Fe_7S_8 .³³ A lattice spacing of 0.26 nm corresponds to (101) and a lattice spacing of 0.30 nm matches with the (110) crystalline plane of FeS .^{34–36} The amorphous carbon layer is also observed by a transmission electron microscope. According to the state-of-the-art literature, this unique carbon layer can protect the polysulfide from dissolving into the organic electrolyte.^{18,37} STEM–EDS elemental mappings (Figure 2e) support the finding that Fe_{1-x}S nanoparticles are surrounded by the carbon layer.

The surface changes of the pristine $\text{Fe}_{1-x}\text{S}/\text{C}$, which was in contact with the LP30 electrolyte, are examined by XPS. The fitting of the Fe 2p_{3/2} spectrum (Figure 3a) indicates that the surfaces of both the $\text{Fe}_{1-x}\text{S}/\text{C}$ and the $\text{Fe}_{1-x}\text{S}/\text{C-LP30-1h}$ materials contain mainly Fe(2+)-S, Fe(3+)-S, and Fe(3+)-O,^{38,39} which correspond to photoelectron peaks at 708.4, 710.5, and 711.6 eV (main peak), respectively.^{40,41} The presence of Fe(3+)-O on the surface of $\text{Fe}_{1-x}\text{S}/\text{C}$ results from the reaction between Fe(3+)-S/Fe(2+)-S and oxygen/water.⁴² Compared with the satellite peak of the pristine $\text{Fe}_{1-x}\text{S}/\text{C}$ at 715.4 eV, there is a broader photoelectron peak

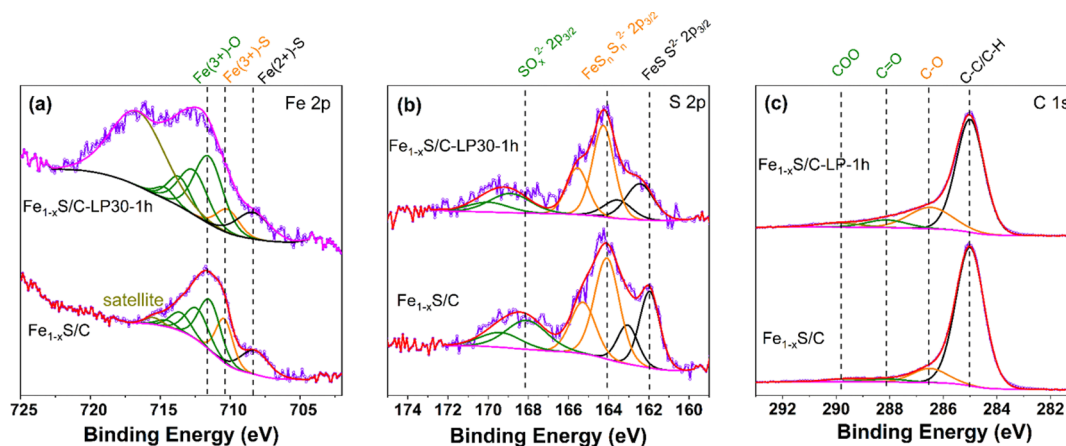


Figure 3. XPS spectra of Fe 2p (a), S 2p (b), and C 1s (c) of the pristine $\text{Fe}_{1-x}\text{S}/\text{C}$ (down) and $\text{Fe}_{1-x}\text{S}/\text{C-LP30-1h}$ (top).

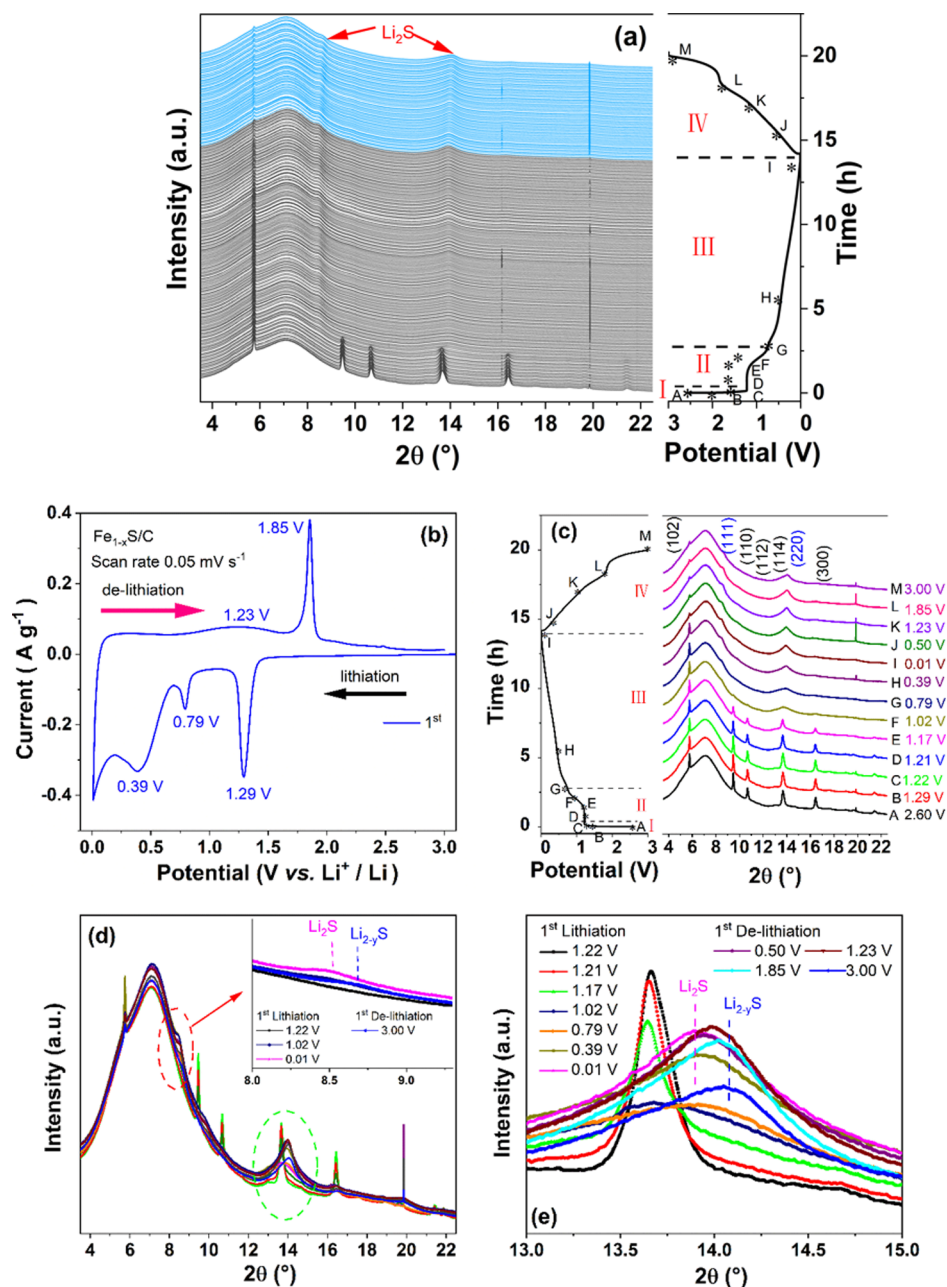


Figure 4. *In operando* synchrotron radiation diffraction patterns of the $\text{Fe}_{1-x}\text{S}/\text{C}$ electrode during the 1st cycle: the XRD reflection patterns and the relative discharging/charging curves (a); relative electrochemical potential profiles; the 1st CV curve of the $\text{Fe}_{1-x}\text{S}/\text{C}$ electrode (b); XRD reflection patterns at the specific potentials (c); the magnification of the reflection (8.5 → 8.7°) (d); and the magnification of the reflection shift (13.9 → 14.1°) during the 1st electrochemical cycling (e).

located at 716.6 eV for the $\text{Fe}_{1-x}\text{S}/\text{C}$ -LP30-1h composite. This unclear photoelectron peak could be attributed to the satellites of $\text{Fe}(2+)/\text{Fe}(3+)$ and the influence of Li^+ -ions on the surface of the pristine $\text{Fe}_{1-x}\text{S}/\text{C}$ material. Regarding the S 2p spectrum in Figure 3b, the photoelectron peaks with the binding energies of 168.1, 162.0, and 164.1 eV are assigned to SO_x^{2-} , S^{2-} of FeS , and S_n^{2-} of FeS_n , respectively.⁴³ In comparison, the intensity of S^{2-} 2p for the pristine $\text{Fe}_{1-x}\text{S}/\text{C}$ slightly decreases the photoelectron peaks and slightly shifts to a higher binding energy after mixing with LP30. The C 1s spectrum displays the C component for both samples: a main peak at 285.0 eV (C–C) and other small peaks at 289.6 eV (O–C=O), 286.4 eV (C–O–C), and 288.0 eV (C=O) in Figure 3c.⁴⁴ After the pristine $\text{Fe}_{1-x}\text{S}/\text{C}$ material comes in contact with LP30 for 1 h,

the intensities of the peaks at 286.4 eV (C–O–C), 288.0 eV (C=O) increase because of the reaction of $\text{Fe}_{1-x}\text{S}/\text{C}$ toward oxygen.

2.2. Investigation of the Structural Changes through *In Operando* Studies. The detailed understanding of the conversion reactions occurring during Li-insertion/de-insertion into the $\text{Fe}_{1-x}\text{S}/\text{C}$ electrode is critical for its further improvement. The structural changes of the $\text{Fe}_{1-x}\text{S}/\text{C}$ electrode are studied by using *in operando* synchrotron radiation diffraction during the 1st lithiation/de-lithiation processes. Figure 4a shows all XRD patterns and the discharge/charge curves of the $\text{Fe}_{1-x}\text{S}/\text{C}$ electrode during the 1st electrochemical process. Figure 4b presents the 1st cyclic voltammetry (CV) curve, three cathodic peaks (1.29,

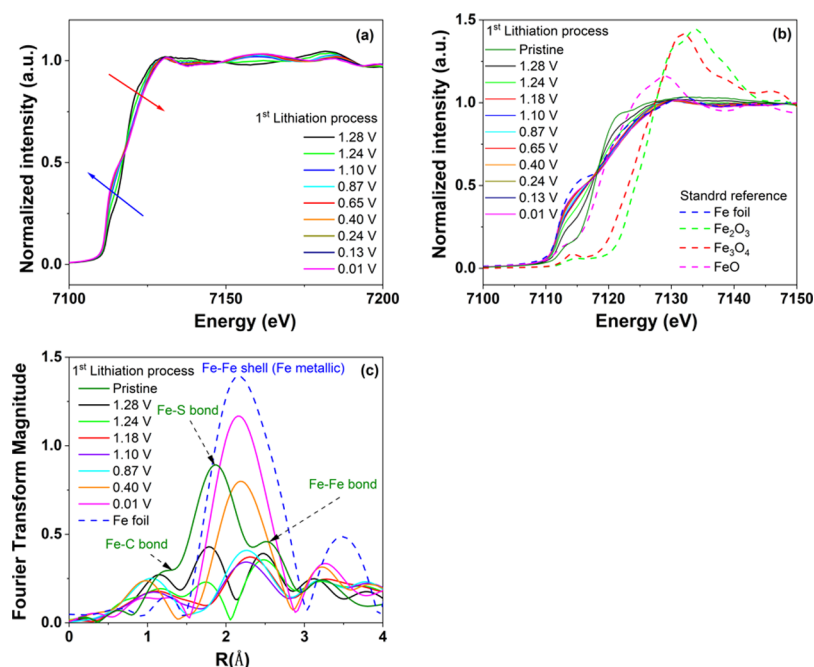


Figure 5. Fe K-edge XANES of the $\text{Fe}_{1-x}\text{S}/\text{C}$ electrode at different potentials (a) and compared with some iron oxide standard references (b). The Fe K-edge FT-EXAFS spectra of the $\text{Fe}_{1-x}\text{S}/\text{C}$ electrode during the 1st lithiation process (c).

0.79, and 0.39 V), and two oxidation peaks (1.23 and 1.85 V). Normally, the plateau occurring in galvanostatic cycling with potential limitation (GCPL) is consistent with cathodic/anodic peaks in the CV curve. One can observe that one plateau (1.22 V) in GCPL and the peak (1.29 V) in the CV curve are not at the identical potential. This small shift is due to the different electrochemical measurement modes: the GCPL (charge/discharge) is performed at a specific current of 0.08 A g^{-1} , while the CV measurements are conducted at 0.05 mV s^{-1} . According to the diffraction peak trend, the potential profile is divided into four regions:

- (I) Region I ($\sim 2.60 \rightarrow \sim 1.22 \text{ V}$): Li^+ insertion process;
- (II) Region II ($\sim 1.22 \rightarrow \sim 0.79 \text{ V}$): conversion step 1;
- (III) Region III ($\sim 0.79 \rightarrow \sim 0.01 \text{ V}$): conversion step 2;
- (IV) Region IV ($\sim 0.01 \rightarrow \sim 3.00 \text{ V}$): de-lithiation process.

During the 1st lithiation process, in region I, a fast drop of the potential from ~ 2.60 to $\sim 1.22 \text{ V}$ occurs. One of the reflection peaks ($9.4\text{--}9.6^\circ$) slightly shifts to a lower 2θ angle (Figure S2a), which is ascribed to Li^+ insertion into $\text{Fe}_{1-x}\text{S}/\text{C}$. In region II, the amorphization process (small plateau at $\sim 1.22 \text{ V}$) leads the intensities of some reflection patterns ($5.7, 9.4, 10.6, 13.6$, and 16.4°) to gradually decrease, which is attributed to the conversion step 1 ($\text{Fe}_{1-x}\text{S} \rightarrow \text{Li}_2\text{Fe}_{1-x}\text{S}_2$), with the formation of metallic Fe^0 (eq 1). The intensity of the reflection at $13.2\text{--}14.0^\circ$ decreases during the 1st lithiation process ($\sim 1.22 \rightarrow \sim 1.02 \text{ V}$), as shown in Figure S2b (Supporting Information). In region III, upon further electrochemical reduction, the intensities mentioned above fade out, which is due to the fact that the $\text{Fe}_{1-x}\text{S}/\text{C}$ material is completely consumed and because synchrotron radiation diffraction does not detect such small-size products.^{45–47} More importantly, two new reflections (8.5 and 13.9°) appear and continuously broaden, which is ascribed to the conversion step 2 with the formation of Li_2S (JCPDS card no. 26-1188) and metallic Fe^0 (eq 2). However, the XRD patterns related to metallic Fe^0 cannot be detected by synchrotron radiation diffraction because of the nanometer size and amorphous structure. The

conversion step 2 is correlated to the small CV peak located at $\sim 0.79 \text{ V}$. One broad cathodic peak at 0.39 V indicates that the solid electrolyte interphase (SEI) is formed.⁴⁸ Figure 4c depicts *in operando* synchrotron radiation diffraction at different potentials during the 1st discharge/charge processes. The changes of reflection intensities, which correspond to phase transition processes, can be observed. In region IV, the reflection intensity (5.7°) continuously decreases, while two broad diffraction peaks shift: $8.5 \rightarrow 8.7^\circ$ and $13.9 \rightarrow 14.1^\circ$. Both shifts correspond to the Li^+ extraction from Li_2S to form Li_{2-y}S (eq 3). This phase transition process ($\text{Li}_2\text{S} \rightarrow \text{Li}_{2-y}\text{S}$) corresponds to the broad anodic peak ($\sim 1.23 \text{ V}$) in Figure 4b. The intensities of the reflection peaks decrease and shift to a higher 2θ angle during the 1st de-lithiation process ($1.23 \rightarrow 3.00 \text{ V}$, Figure 4e), which is due to the Li^+ -ion extraction from Li_2S resulting in a decrease in the unit cell of Li_2S . The pronounced oxidation peak ($\sim 1.85 \text{ V}$) is consistent with the conversion of Fe^0 and Li_2S to $\text{Li}_{2-y}\text{Fe}_{1-x}\text{S}_2$ ($0.5 < x < 0.8$, eq 4).⁹ This peak is consistent with the small plateau observed in the discharging/charging processes (Figure 4a). The oxidation of Fe^0 and Li_2S does not form the initial Fe_{1-x}S material, which is confirmed by the absence of these peaks at $\sim 3.00 \text{ V}$ (1st de-lithiation state). The interconnected carbon microspheres, which surround the Fe_{1-x}S structure, reduce the contact between the Fe_{1-x}S material and the electrolyte and therefore prevent the products, such as Li_2S and $\text{Li}_{2-y}\text{Fe}_{1-x}\text{S}_2$ ($0.5 < x < 0.8$), from dissolving in the electrolyte. The phase transition from Li_2S to Li_{2-y}S is not detected in previous findings. After the 1st de-lithiation process, amorphous lithiated iron sulfide nanoparticles are embedded within the remaining Li_2S matrix.^{49,50} The reflection peaks located at $19\text{--}20^\circ$ are attributed to copper mesh (the current collector and holder $\text{Fe}_{1-x}\text{S}/\text{C}$ active material). Because Cu mesh is not a polycrystalline material, the poor statistics cause random errors in the observed diffraction peak intensities. A broad reflection shift ($8.5 \rightarrow 8.7^\circ$) can be observed in Figure 4d (inset zoom Figure). Figure 4e shows the magnification of the reflection

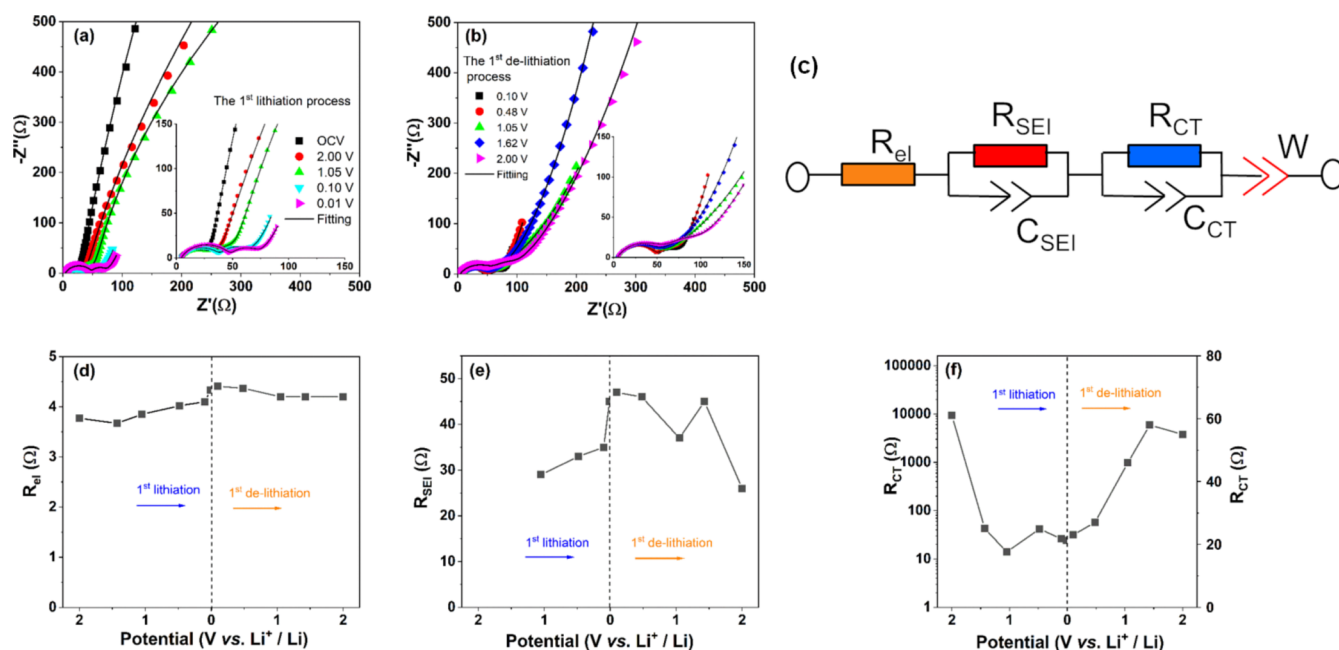
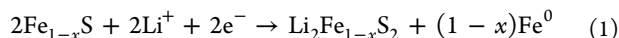


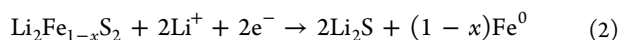
Figure 6. Nyquist plots of the $\text{Fe}_{1-x}\text{S}/\text{C}$ electrode obtained from EIS measurements (the zoom figures show the Nyquist plots in the high-middle frequency region): (a) lithiation process OCV \sim 0.01 V; (b) de-lithiation process \sim 0.01 to \sim 2.00 V; (c) the equivalent circuit used for fitting the EIS experiment data; (d) electrolyte resistance R_{el} ; (e) SEI resistance R_{SEI} ; and (f) charge-transfer resistance R_{CT} .

shift ($13.9 \rightarrow 14.1^\circ$) at some chosen potentials. During the conversion reaction (from ~ 0.79 to ~ 0.01 V), the reflection becomes broader, the intensity increases, and the peak shifts to a higher 2θ angle. When the potential changes from ~ 0.01 to ~ 3.00 V, the intensities of the broad reflection patterns decline and the peak continuously moves to a higher 2θ angle. Based on the above-described analysis, the electrochemical reaction during the 1st cycle can be proposed as

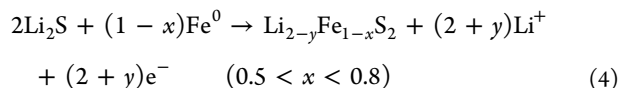
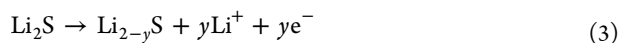
Conversion step 1: (from ~ 1.22 V to ~ 0.79 V)



Conversion step 2: (from ~ 0.79 V to ~ 0.01 V)



De-lithiation process: (from ~ 0.01 V to ~ 3.00 V)



To further study the local environment and electronic transitions of the $\text{Fe}_{1-x}\text{S}/\text{C}$ electrode during the first lithiation/de-lithiation processes, *in operando* XAS was applied. The Fe K-edge X-ray absorption near-edge structure (XANES) of the $\text{Fe}_{1-x}\text{S}/\text{C}$ electrode (Figure 5a) presents a continuous move to lower edge energy (blue arrow) together with the changing edge slope (red arrow), corresponding to the decrease of the oxidation state of Fe and dramatically structural changes ($\sim 1.28 \rightarrow 0.01$ V). The conversion reaction of the Fe_{1-x}S material can also be proved by the appearance of several isosbestic points in all regions of the spectra. In comparison with some standard reference samples in Figure 5b, the valence states of Fe at each state can be determined quantitatively. The oxidation state of the pristine $\text{Fe}_{1-x}\text{S}/\text{C}$ is Fe^{2+} , confirmed by the spectrum, which is very near to one of the FeO standard

references. Clearly, in the potential region between OCV and ~ 0.01 V, the spectrum shifts from FeO to the Fe foil reference. This phenomenon is due to the progressive reduction of Fe_{1-x}S upon lithium insertion. During the 1st lithiation process, the magnitude of Fourier transforms (FT) of Fe K-edge extended X-ray absorption fine structure (EXAFS) spectra of $\text{Fe}_{1-x}\text{S}/\text{C}$ is presented in Figure 5c. The FT-EXAFS peak of the pristine material (OCV) at 1.86 \AA can be assigned to a Fe–S bond. The FT-EXAFS peak at 2.55 \AA could be attributed to the Fe–Fe bond in the Fe_{1-x}S material. Additionally, the FT-EXAFS peak at 1.38 \AA can be fitted as the Fe–C bond.^{51,52} During the reduction process (OCV $\rightarrow \sim 1.28 \text{ V} \rightarrow \sim 1.24 \text{ V}$), the above-mentioned three FT-EXAFS peaks become weaker and weaker, which is because the $\text{Fe}_{1-x}\text{S}/\text{C}$ structure gradually deforms as more Li^+ -ions insert. The newly appeared peaks (after $\sim 1.18 \text{ V}$) at 2.2 \AA ⁴⁵ are attributed to the Fe–Fe coordination shell of the metallic Fe^0 . The amplitude of the peaks related to metallic Fe^0 at $\sim 0.01 \text{ V}$ is smaller than one of the Fe foil references. This small discrepancy is due to the fact that the Fe foil reference has a body-centered cubic (bcc) structure; in comparison, the formed nanometer-sized metallic Fe^0 is amorphous.^{53,54}

2.3. EIS and Morphological Characteristic Evolution during the 1st Cycle. To further investigate the charge-transfer kinetics and resistive contributions during the 1st cycle, EIS measurements are performed and presented in Figure 6. Figure 6a,b displays the experimental and fitted spectra obtained at various potentials. The zoom in the high-to-middle frequency region (from 190 kHz to 218 mHz) is displayed in Figure 6a,b. The equivalent circuit used for fitting the Nyquist plot is shown in Figure 6c. The equivalent circuit is described as $R_{\text{el}}(R_{\text{SEI}}C_{\text{SEI}})(R_{\text{CT}}C_{\text{CT}})W$ in Boukamp's notation.⁵⁵ In detail, R_{el} stands for the electrolyte resistance; R_{el} is the intercept of the Nyquist plot at the Z' real axis in the high-frequency region.⁴⁵ The first semicircle in the high-frequency (H–F) region (from 190 kHz to 27 Hz) is ascribed

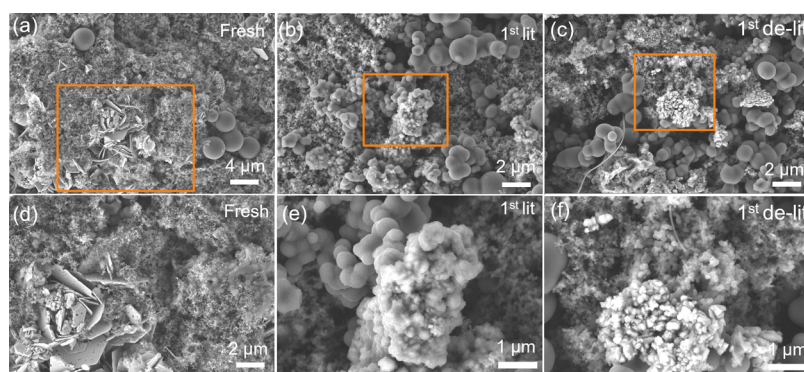


Figure 7. Surface morphology changes of $\text{Fe}_{1-x}\text{S}/\text{C}$ electrodes at different states: fresh electrode (a,d); the 1st lithiation electrode (b,e); the 1st de-lithiation electrode (c,f).

to the Li^+ -ion movement through the SEI layer (R_{SEI}) and the associated capacitance (C_{SEI}). The second semicircle in the middle-frequency (M-F) region (from 27 Hz to 218 mHz) is attributed to the charge-transfer resistance (R_{CT}) and the double-layer capacitance (C_{CT}). W represents the Warburg impedance in the low-frequency (L-F) region (from 18 to 218 mHz).^{56–59} Figure S3 (Supporting Information) shows one fitted Nyquist plot at 0.48 V during lithiation. Figure 6d displays the variations of R_{el} during the 1st reduction process. The average R_{el} value during the 1st de-lithiation process is higher than that during the 1st lithiation process. R_{el} slightly increases from 3.8 to 4.3 Ω during the 1st lithiation process, and R_{el} decreases from 4.4 to 4.2 Ω during the 1st de-lithiation process. The changes of R_{el} are due to the SEI formation process consuming Li^+ -ions and organic compounds from the electrolyte.⁶⁰ The changes of R_{SEI} at various potentials are shown in Figure 6e. During the 1st lithiation process ($\sim 1.04 \rightarrow \sim 0.01$ V), R_{SEI} increases from 30 to 45 Ω , which is due to the formation of SEI at lower potential upon Li^+ insertion. During the 1st de-lithiation process ($\sim 0.10 \rightarrow \sim 2.00$ V), R_{SEI} declines from 47 to 26 Ω . The above-mentioned variation of the R_{SEI} indicates that the SEI film is formed during the Li^+ -ion insertion process, and it is decomposed during Li^+ -ion extraction.^{61,62} Additionally, at the beginning of the 1st lithiation process (~ 2.00 and ~ 1.05 V), the Nyquist plots display one semicircle in the high-frequency region (from 190 kHz to 27 Hz). On the other hand, when the potentials are ~ 0.10 and ~ 0.01 V, the Nyquist plots are composed of two semicircles (the one at higher frequencies corresponding to R_{SEI}), which further confirm that the SEI is formed at low potentials. Additionally, the slope of the $\text{Fe}_{1-x}\text{S}/\text{C}$ electrode declines with the decrease of the potential (from ~ 2.00 to ~ 0.01 V) in the low-frequency region (from 18 mHz to 218 mHz), which implies a fast Li^+ mobility as more Li^+ -ions insert. During the 1st lithiation process ($\sim 2.00 \rightarrow \sim 1.05$ V), the R_{CT} sharply declines from 9359 to 14 Ω (Figure 6f), and then the R_{CT} increases again from 14 to 42 Ω with a decrease in potential ($\sim 1.05 \rightarrow \sim 0.48$ V). The much lower R_{CT} values at the potential of 1.43–1.05 V is due to the initial Li^+ -ion insertion process ($\text{Fe}_{1-x}\text{S} \rightarrow \text{Li}_2\text{Fe}_{1-x}\text{S}_2$), accompanied by fast charge-transfer kinetics. The charge-transfer kinetics becomes slow during the subsequent conversion reaction ($\text{Li}_2\text{Fe}_{1-x}\text{S}_2 \rightarrow \text{Li}_2\text{S} + \text{Fe}^0$), which also includes the formation of the SEI layer, as observed by the increase of R_{CT} at 1.05–0.48 V. During the 1st de-lithiation process, R_{CT} increases to 58 Ω (~ 1.43 V). The increase of R_{CT} is caused by Li^+ -ion extraction from a less conductive SEI. By increasing the potential to 2 V, the R_{CT}

decreases to 55 Ω , indicating that the SEI decomposes at a high potential. Zhao *et al.*⁴⁷ demonstrated similar findings in another type of conversion materials.

Figure 7 presents the surface morphology changes of the fresh $\text{Fe}_{1-x}\text{S}/\text{C}$ electrode and electrodes at the 1st lithiation and de-lithiation states. The fresh electrode (Figure 7a,d) is composed of homogeneously distributed Fe_{1-x}S (50–60 nm) interconnected with carbon spheres (1–2 μm). The surface morphology of the electrodes after the 1st lithiation (Figure 7b,e) and de-lithiation (Figure 7c,f) has an irreversible alteration-like aggregation due to active material pulverization. This is assigned to the Li^+ insertion/extraction into/from the active material, resulting in notable roughness increase and amplification of the converted grains.^{63,64} As it can be observed in the 1st de-lithiated electrode, more cavities are present in comparison with the 1st lithiated electrode, indicating that Fe_{1-x}S pulverizes already after the first cycle. These microstructural alternations provide new reaction sites in the $\text{Fe}_{1-x}\text{S}/\text{C}$ electrodes, facilitating the electrochemical reaction process in the following cycles and SEI film formation.⁶⁴

3. CONCLUSIONS

For the first time, the lithium storage mechanism related to the $\text{Fe}_{1-x}\text{S}/\text{C}$ anode was tracked in real time during the 1st lithiation/de-lithiation processes. Electronic changes and structural alterations are investigated by combining *in operando* analytic techniques such as synchrotron radiation diffraction and XAS. The analysis of these data reveals the occurrence of phase transition ($\text{Fe}_{1-x}\text{S} \rightarrow \text{Li}_2\text{Fe}_{1-x}\text{S}_2 \rightarrow \text{Fe}^0 + \text{Li}_2\text{S}$) during the 1st lithiation process. *In operando* XAS confirms the redox reaction of $\text{Fe}^{2+} + 2\text{e}^- \rightleftharpoons \text{Fe}^0$ and the Fe K-edge XAS transformation process. During the 1st de-lithiation process, Fe^0 and Li_2S convert to $\text{Li}_{2-y}\text{Fe}_{1-x}\text{S}_2$ and Li^+ is extracted from Li_2S to form Li_{2-y}S . This is the first time that the phase transition from Li_2S to Li_{2-y}S is detected. After the 1st de-lithiation process, amorphous lithiated iron sulfide nanoparticles are embedded within the remaining Li_2S matrix. HR-TEM proves the presence of Fe_7S_8 and FeS in $\text{Fe}_{1-x}\text{S}/\text{C}$ nanocomposites. The amorphous carbon layer is also observed by TEM. XPS also confirms the presence of carbon, which provides an electronic pathway for fast charge transfer and buffers the lithiation/de-lithiation-induced volume variation. The kinetic process demonstrates that the SEI film is formed during the Li^+ -ion insertion process and then it is decomposed during Li^+ -ion extraction. Furthermore, *ex situ* SEM shows that the surface morphology has an irreversible alteration due to Fe_{1-x}S pulverization. These results can shed light on the

lithium storage mechanism for the conversion-type material, especially for the iron-deficient sulfides.

4. EXPERIMENTAL SECTION

4.1. Synthesis of FeS Nanosheets and the Fe_{1-x}S/C Composite Material. The Fe_{1-x}S/C composite material was prepared *via* two steps: a hydrothermal method and a subsequent sintering process, as depicted in our previous work.²⁶

4.2. Material Characterization. The structural properties of the products are investigated by XRD. The pristine Fe_{1-x}S/C material was measured at the Materials Science (MS) beamline, Swiss Light Source ($\lambda = 0.49310$ Å, 25 keV).⁶⁵ Fe_{1-x}S/C-LP30-1h was performed with Mo K α_1 radiation ($\lambda = 0.709300$ Å). The crystal structure and phase fraction are obtained from the Rietveld refinement.⁶⁶ The surface morphology of the pristine Fe_{1-x}S/C material and the cycled electrodes are observed by SEM (Carl Zeiss SMT AG). The elemental mapping of the pristine Fe_{1-x}S/C material is confirmed by EDS (Bruker, QUANTAX 400 SDD).²⁶ STEM and HR-TEM (FEI company, Titan 80–300) are used to further visualize the crystalline structure *via* a Gatan US1000 slow-scan CCD camera.⁸ XPS is conducted on the K-Alpha⁺ XPS spectrometer (Thermo-Fisher Scientific, East Grinstead, U.K.).²⁶ Data acquisition and processing are carried out using the Thermo Advantage software.⁶⁷ The C 1s peak with a binding energy of 285.0 eV is used as a reference.⁴⁷

4.3. Electrochemical Characterization. The detailed process for preparing the working electrodes is described in our previous publication.²⁶ The working electrode with low mass loading (0.7 mg cm⁻², a diameter of 7 mm) is used for the electrochemical impedance study. The working electrodes for CV, rate performance, and galvanostatic charging/discharging measurements have a higher average mass loading and thickness (1.5–2.0 mg cm⁻², 75 μ m). The counter electrode/reference electrode is lithium chips (Alfa Aesar). The separators (Whatman GF/D, a diameter of 12 mm) were vacuum-dried before assembling the cells. The commercial LP30 (BASF, Germany) was used as an electrolyte. The multichannel potentiostat (VMP3, Bio-Logic) was used for electrochemical measurements (CV, rate performance, charging/discharging, and electrochemical impedance).²⁶ The potential range used was as follows: 0.01–3.0 V *vs* Li⁺/Li. All electrochemical measurements were performed using a three-electrode Swagelok-type cell. The half-cell was prepared in a glovebox (MBraun, O₂ and H₂O \leq 0.5 ppm).²⁶ All cells were kept in a climate chamber (Binder GmbH) at room temperature. For the EIS measurements (from 10 mHz to 500 kHz), the half-cell was equilibrated 3 h before running the electrochemical impedance. The Nyquist plots were fitted and resistance value was obtained by the Relaxis 3 software (rhd Instruments, Germany).²⁶

4.4. In Operando Characterization. For *in operando* measurements, the working electrodes were mixed with the pristine Fe_{1-x}S/C material (70 wt %), carbon black (Super P, TIMCAL Ltd. 20 wt %), and polytetrafluoroethylene beads (Aldrich, 10 wt %). The above mixture (mass loading of 2.5–3.6 mg cm⁻²) was pressed on the center of copper mesh.⁸ A CR2025 coin cell with glass windows was used for synchrotron radiation diffraction and a CR2025 coin cell with Kapton windows was used to perform XAS measurements.

The cell was charged/discharged at 80 mA g⁻¹ (synchrotron radiation diffraction) and 100 mA g⁻¹ (XAS) at 0.01–3.0 V *vs* Li⁺/Li. *In operando* synchrotron radiation diffraction was performed at the MS beamline, Swiss Light Source.⁶⁵ LaB₆ and Si are two standard references used for calibration. *In operando* XAS was carried on the P65 beamline, PETRA III, German Electron Synchrotron (DESY, Hamburg). Fe₂O₃, FeO, Fe₃O₄, and metallic Fe foil were employed as standard materials. The XAS spectra were analyzed by the Demeter software package.⁶⁸

■ ASSOCIATED CONTENT

Supporting Information

The Supporting Information is available free of charge at <https://pubs.acs.org/doi/10.1021/acsami.0c15500>.

EDS elemental maps, structural characteristics of the pristine Fe_{1-x}S material, magnification of the reflection during the 1st lithiation process, and Nyquist plot obtained at the 1st lithiation 0.48 V of the Fe_{1-x}S/C electrode (PDF)

■ AUTHOR INFORMATION

Corresponding Author

Sonia Dsoke – Institute for Applied Materials (IAM), Eggenstein-Leopoldshafen 76344, Germany; Helmholtz Institute Ulm for Electrochemical Energy Storage (HIU), Ulm 89081, Germany; orcid.org/0000-0001-9295-2110; Email: sonia.dsoke@kit.edu

Authors

Chengping Li – Institute for Applied Materials (IAM), Eggenstein-Leopoldshafen 76344, Germany
Angelina Sarapulova – Institute for Applied Materials (IAM), Eggenstein-Leopoldshafen 76344, Germany
Kristina Pfeifer – Institute for Applied Materials (IAM), Eggenstein-Leopoldshafen 76344, Germany
Xianlin Luo – Institute for Applied Materials (IAM), Eggenstein-Leopoldshafen 76344, Germany; Karlsruhe Nano Micro Facility (KNMF), Karlsruhe Institute of Technology (KIT), Eggenstein-Leopoldshafen 76344, Germany
Nicola Pietro Maria Casati – Paul Scherrer Institute, Villigen PSI 5232, Switzerland; orcid.org/0000-0002-4206-9239
Edmund Welter – Deutsches Elektronen-Synchrotron DESY, A Research Centre of the Helmholtz Association, Hamburg D-22607, Germany
Georgian Melinte – Institute of Nanotechnology (INT), Eggenstein-Leopoldshafen 76344, Germany
Qiang Fu – Institute for Applied Materials (IAM), Eggenstein-Leopoldshafen 76344, Germany; orcid.org/0000-0002-2507-5477

Complete contact information is available at: <https://pubs.acs.org/doi/10.1021/acsami.0c15500>

Notes

The authors declare no competing financial interest.

■ ACKNOWLEDGMENTS

C.L. acknowledges the financial support from the China Scholarship Council (CSC grant number: 201707030004) during the PhD study in KIT. We thank Prof. Dr. Helmut Ehrenberg, who agreed and supported this project. We would also like to acknowledge Dr. Florian Sigel (IAM-ESS) for the Beam-time (Proposal-ID 20190924, MS-Powder beamline) and DESY (Hamburg, Germany) for providing experimental facilities. This research work contributes to the research performed at CELEST (Center for Electrochemical Energy Storage Ulm-Karlsruhe).

■ REFERENCES

- (1) Li, M.; Lu, J.; Chen, Z.; Amine, K. 30 Years of Lithium-Ion Batteries. *Adv. Mater.* **2018**, *30*, 1800561.
- (2) Bresser, D.; Passerini, S.; Scrosati, B. Leveraging Valuable Synergies by Combining Alloying and Conversion for Lithium-Ion Anodes. *Energy Environ. Sci.* **2016**, *9*, 3348–3367.
- (3) Lin, Y.; Qiu, Z.; Li, D.; Ullah, S.; Hai, Y.; Xin, H.; Liao, W.; Yang, B.; Fan, H.; Xu, J.; Zhu, C. NiS₂/CoS₂ Nanocrystals Encapsulated in N-Doped Carbon Nanocubes for High Performance Lithium/Sodium Ion Batteries. *Energy Storage Mater.* **2018**, *11*, 67–74.

- (4) Ma, Y.; Ma, Y.; Bresser, D.; Ji, Y.; Geiger, D.; Kaiser, U.; Streb, C.; Varzi, A.; Passerini, S. Cobalt Disulfide Nanoparticles Embedded in Porous Carbonaceous Micro-Polyhedrons Interlinked by Carbon Nanotubes for Superior Lithium and Sodium Storage. *ACS Nano* **2018**, *12*, 7220–7231.
- (5) Zhang, Y.; Zhu, P.; Huang, L.; Xie, J.; Zhang, S.; Cao, G.; Zhao, X. Few-Layered SnS_2 on Few-Layered Reduced Graphene Oxide as Na-Ion Battery Anode with Ultralong Cycle Life and Superior Rate Capability. *Adv. Funct. Mater.* **2015**, *25*, 481–489.
- (6) Evans, T.; Piper, D. M.; Kim, S. C.; Han, S. S.; Bhat, V.; Oh, K. H.; Lee, S.-H. Ionic Liquid Enabled FeS_2 for High-Energy-Density Lithium-Ion Batteries. *Adv. Mater.* **2014**, *26*, 7386–7392.
- (7) Stephenson, T.; Li, Z.; Olsen, B.; Mitlin, D. Lithium Ion Battery Applications of Molybdenum Disulfide (MoS_2) Nanocomposites. *Energy Environ. Sci.* **2014**, *7*, 209–231.
- (8) Tian, G.; Zhao, Z.; Sarapulova, A.; Das, C.; Zhu, L.; Liu, S.; Missiul, A.; Welter, E.; Maibach, J.; Dsoke, S. Understanding the Li-Ion Storage Mechanism in a Carbon Compositized Zinc Sulfide Electrode. *J. Mater. Chem. A* **2019**, *7*, 15640–15653.
- (9) Wu, B.; Song, H.; Zhou, J.; Chen, X. Iron Sulfide-Embedded Carbon Microsphere Anode Material with High-Rate Performance for Lithium-Ion Batteries. *Chem. Commun.* **2011**, *47*, 8653.
- (10) Xu, C.; Zeng, Y.; Rui, X.; Xiao, N.; Zhu, J.; Zhang, W.; Chen, J.; Liu, W.; Tan, H.; Hng, H. H.; Yan, Q. Controlled Soft-Template Synthesis of Ultrathin C@FeS Nanosheets with High-Li-Storage Performance. *ACS Nano* **2012**, *6*, 4713–4721.
- (11) Li, J.; Wang, L.; Li, L.; Lv, C.; Zlatovskiy, I. V.; Han, W. Metal Sulfides@Carbon Microfiber Networks for Boosting Lithium Ion/Sodium Ion Storage via a General Metal–Aspergillus Niger Bioleaching Strategy. *ACS Appl. Mater. Interfaces* **2019**, *11*, 8072–8080.
- (12) Huang, A.; Wang, Q.; Ma, Z.; Rui, K.; Huang, X.; Zhu, J.; Huang, W. Surface Anionization of Self-Assembled Iron Sulfide Hierarchitectures to Enhance Capacitive Storage for Alkaline-Metal-Ion Batteries. *ACS Appl. Mater. Interfaces* **2019**, *11*, 39991–39997.
- (13) Haridas, A. K.; Heo, J.; Liu, Y.; Ahn, H.-J.; Zhao, X.; Deng, Z.; Agostini, M.; Matic, A.; Cho, K.-K.; Ahn, J.-H. Boosting High Energy Density Lithium-Ion Storage via the Rational Design of an FeS -Incorporated Sulfurized Polyacrylonitrile Fiber Hybrid Cathode. *ACS Appl. Mater. Interfaces* **2019**, *11*, 29924–29933.
- (14) Hou, B.-H.; Wang, Y.-Y.; Guo, J.-Z.; Zhang, Y.; Ning, Q.-L.; Yang, Y.; Li, W.-H.; Zhang, J.-P.; Wang, X.-L.; Wu, X.-L. A Scalable Strategy To Develop Advanced Anode for Sodium-Ion Batteries: Commercial Fe_3O_4 -Derived $\text{Fe}_3\text{O}_4/\text{FeS}$ with Superior Full-Cell Performance. *ACS Appl. Mater. Interfaces* **2018**, *10*, 3581–3589.
- (15) Pfeifer, K.; Arnold, S.; Budak, Ö.; Luo, X.; Presser, V.; Ehrenberg, H.; Dsoke, S. Choosing the Right Carbon Additive Is of Vital Importance for High-Performance Sb-Based Na-Ion Batteries. *J. Mater. Chem. A* **2020**, *8*, 6092–6104.
- (16) Li, D.; Sun, Y.; Chen, S.; Yao, J.; Zhang, Y.; Xia, Y.; Yang, D. Highly Porous FeS/Carbon Fibers Derived from Fe-Carrageenan Biomass: High-Capacity and Durable Anodes for Sodium-Ion Batteries. *ACS Appl. Mater. Interfaces* **2018**, *10*, 17175–17182.
- (17) Wei, X.; Li, W.; Shi, J.-a.; Gu, L.; Yu, Y. FeS@C on Carbon Cloth as Flexible Electrode for Both Lithium and Sodium Storage. *ACS Appl. Mater. Interfaces* **2015**, *7*, 27804–27809.
- (18) Fei, L.; Lin, Q.; Yuan, B.; Chen, G.; Xie, P.; Li, Y.; Xu, Y.; Deng, S.; Smirnov, S.; Luo, H. Reduced Graphene Oxide Wrapped FeS Nanocomposite for Lithium-Ion Battery Anode with Improved Performance. *ACS Appl. Mater. Interfaces* **2013**, *5*, 5330–5335.
- (19) Jones, C. H. W.; Kovacs, P. E.; Sharma, R. D.; McMillan, R. S. Iron-57 Moessbauer Spectroscopy of the Iron Monosulfide Cathode in the Lithium/Iron Monosulfide Battery System. *J. Phys. Chem.* **1990**, *94*, 4325–4329.
- (20) Wang, C.; Lan, M.; Zhang, Y.; Bian, H.; Yuen, M.-F.; Ostrikov, K.; Jiang, J.; Zhang, W.; Li, Y. Y.; Lu, J. $\text{Fe}_{1-x}\text{S}/\text{C}$ Nanocomposites from Sugarcane Waste-Derived Microporous Carbon for High-Performance Lithium Ion Batteries. *Green Chem.* **2016**, *18*, 3029–3039.
- (21) Liu, Y.; Zhong, M.; Kong, L.; Li, A.; Sun, X.; Wang, D.; Bu, X.-H. $\text{Fe}_{1-x}\text{S}/\text{Nitrogen}$ and Sulfur Co-Doped Carbon Composite Derived from a Nanosized Metal–Organic Framework for High-Performance Lithium-Ion Batteries. *Inorg. Chem. Front.* **2019**, *6*, 50–56.
- (22) Xiao, Y.; Hwang, J.-Y.; Belharouak, I.; Sun, Y.-K. Na Storage Capability Investigation of a Carbon Nanotube-Encapsulated Fe_{1-x}S Composite. *ACS Energy Lett.* **2017**, *2*, 364–372.
- (23) Belzile, N.; Chen, Y.-W.; Cai, M.-F.; Li, Y. A Review on Pyrrhotite Oxidation. *J. Geochem. Explor.* **2004**, *84*, 65–76.
- (24) de Villiers, J. P. R.; Liles, D. C.; Becker, M. The Crystal Structure of a Naturally Occurring SC Pyrrhotite from Sudbury, Its Chemistry, and Vacancy Distribution. *Am. Mineral.* **2009**, *94*, 1405–1410.
- (25) Han, W.; Gao, M. Investigations on Iron Sulfide Nanosheets Prepared via a Single-Source Precursor Approach. *Cryst. Growth Des.* **2008**, *8*, 1023–1030.
- (26) Li, C.; Sarapulova, A.; Pfeifer, K.; Dsoke, S. Effect of Continuous Capacity Rising Performed by $\text{FeS}/\text{Fe}_3\text{C}/\text{C}$ Composite Electrodes for Lithium-Ion Batteries. *ChemSusChem* **2020**, *13*, 986–995.
- (27) Multani, R. S.; Waters, K. E. A Review of the Physicochemical Properties and Flotation of Pyrrhotite Superstructures ($4\text{C-Fe}_7\text{S}_8/\text{SC-Fe}_9\text{S}_{10}$) in Ni-Cu Sulphide Mineral Processing. *Can. J. Chem. Eng.* **2018**, *96*, 1185–1206.
- (28) Belzile, N.; Chen, Y.-W.; Cai, M.-F.; Li, Y. A Review on Pyrrhotite Oxidation. *J. Geochem. Explor.* **2004**, *84*, 65–76.
- (29) Burda, C.; Chen, X.; Narayanan, R.; El-Sayed, M. A. Chemistry and Properties of Nanocrystals of Different Shapes. *Chem. Rev.* **2005**, *105*, 1025–1102.
- (30) Becker, M.; Villiers, J. d.; Bradshaw, D. The Flotation of Magnetic and Non-Magnetic Pyrrhotite from Selected Nickel Ore Deposits. *Miner. Eng.* **2010**, *23*, 1045–1052.
- (31) Chen, Y.-H.; Chen, Y.-H.; Hsu, W.-D.; Chang, Y.-C.; Sheu, H.-S.; Lee, J.-J.; Lin, S.-K. Using the High-Temperature Phase Transition of Iron Sulfide Minerals as an Indicator of Fault Slip Temperature. *Sci. Rep.* **2019**, *9*, 7950.
- (32) Haines, C. R. S.; Howard, C. J.; Harrison, R. J.; Carpenter, M. A. Group-Theoretical Analysis of Structural Instability, Vacancy Ordering and Magnetic Transitions in the System Troilite (FeS)–Pyrrhotite (Fe_{1-x}S). *Acta Crystallogr., Sect. B: Struct. Sci., Cryst. Eng. Mater.* **2019**, *75*, 1208–1224.
- (33) Wang, Y.-X.; Yang, J.; Chou, S.-L.; Liu, H. K.; Zhang, W.; Zhao, D.; Dou, S. X. Uniform Yolk-Shell Iron Sulfide–Carbon Nanospheres for Superior Sodium–Iron Sulfide Batteries. *Nat. Commun.* **2015**, *6*, 8689.
- (34) Zhu, C.; Wen, Y.; van Aken, P. A.; Maier, J.; Yu, Y. High Lithium Storage Performance of FeS Nanodots in Porous Graphitic Carbon Nanowires. *Adv. Funct. Mater.* **2015**, *25*, 2335–2342.
- (35) Xu, Y.; Li, W.; Zhang, F.; Zhang, X.; Zhang, W.; Lee, C.-S.; Tang, Y. In Situ Incorporation of FeS Nanoparticles/Carbon Nanosheets Composite with an Interconnected Porous Structure as a High-Performance Anode for Lithium Ion Batteries. *J. Mater. Chem. A* **2016**, *4*, 3697–3703.
- (36) Yang, W.; Zhao, H.; Chen, L.; Fang, C.; Rui, Z.; Yang, L.; Wan, H.; Liu, J.; Zhou, Y.; Wang, P.; Zou, Z. Ferrous Sulfide-Assisted Hollow Carbon Spheres as Sulfur Host for Advanced Lithium-Sulfur Batteries. *Chem. Eng. J.* **2017**, *326*, 1040–1047.
- (37) Ma, Y.; Asfaw, H. D.; Edström, K. A General Method to Fabricate Free-Standing Electrodes: Sulfonate Directed Synthesis and Their Li^+ Storage Properties. *Chem. Mater.* **2015**, *27*, 3957–3965.
- (38) Boursiquot, S.; Mullet, M.; Ehrhardt, J.-J. XPS Study of the Reaction of Chromium (VI) with Mackinawite (FeS). *Surf. Interface Anal.* **2002**, *34*, 293–297.
- (39) Mullet, M.; Boursiquot, S.; Abdelmoula, M.; Génin, J.-M.; Ehrhardt, J.-J. Surface Chemistry and Structural Properties of Mackinawite Prepared by Reaction of Sulfide Ions with Metallic Iron. *Geochim. Cosmochim. Acta* **2002**, *66*, 829–836.

- (40) Thomas, J. E.; Jones, C. F.; Skinner, W. M.; Smart, R. S. C. The Role of Surface Sulfur Species in the Inhibition of Pyrrhotite Dissolution in Acid Conditions. *Geochim. Cosmochim. Acta* **1998**, *62*, 1555–1565.
- (41) Lan, Y.; Butler, E. C. Iron-Sulfide-Associated Products Formed during Reductive Dechlorination of Carbon Tetrachloride. *Environ. Sci. Technol.* **2016**, *50*, 5489–5497.
- (42) Kim, E.-J.; Kim, J.-H.; Azad, A.-M.; Chang, Y.-S. Facile Synthesis and Characterization of Fe/FeS Nanoparticles for Environmental Applications. *ACS Appl. Mater. Interfaces* **2011**, *3*, 1457–1462.
- (43) Wang, Q.; Zhang, W.; Guo, C.; Liu, Y.; Wang, C.; Guo, Z. In Situ Construction of 3D Interconnected FeS@Fe₃C@Graphitic Carbon Networks for High-Performance Sodium-Ion Batteries. *Adv. Funct. Mater.* **2017**, *27*, 1703390.
- (44) López, G. P.; Castner, D. G.; Ratner, B. D. XPS O 1s Binding Energies for Polymers Containing Hydroxyl, Ether, Ketone and Ester Groups. *Surf. Interface Anal.* **1991**, *17*, 267–272.
- (45) Li, C.; Sarapulova, A.; Zhao, Z.; Fu, Q.; Trouillet, V.; Missiul, A.; Welter, E.; Dsoke, S. Understanding the Lithium Storage Mechanism in Core–Shell Fe₂O₃@C Hollow Nanospheres Derived from Metal–Organic Frameworks: An In Operando Synchrotron Radiation Diffraction and in Operando X-Ray Absorption Spectroscopy Study. *Chem. Mater.* **2019**, *31*, 5633–5645.
- (46) Permien, S.; Indris, S.; Hansen, A.-L.; Scheuermann, M.; Zahn, D.; Schürmann, U.; Neubüser, G.; Kienle, L.; Yegudin, E.; Bensch, W. Elucidation of the Conversion Reaction of CoMnFeO₄ Nanoparticles in Lithium Ion Battery Anode via Operando Studies. *ACS Appl. Mater. Interfaces* **2016**, *8*, 15320–15332.
- (47) Zhao, Z.; Tian, G.; Sarapulova, A.; Trouillet, V.; Fu, Q.; Geckle, U.; Ehrenberg, H.; Dsoke, S. Elucidating the Energy Storage Mechanism of ZnMn₂O₄ as Promising Anode for Li-Ion Batteries. *J. Mater. Chem. A* **2018**, *6*, 19381–19392.
- (48) Xing, C.; Zhang, D.; Cao, K.; Zhao, S.; Wang, X.; Qin, H.; Liu, J.; Jiang, Y.; Meng, L. In Situ Growth of FeS Microsheet Networks with Enhanced Electrochemical Performance for Lithium-Ion Batteries. *J. Mater. Chem. A* **2015**, *3*, 8742–8749.
- (49) Ma, Q.; Song, H.; Zhuang, Q.; Liu, J.; Zhang, Z.; Mao, C.; Peng, H.; Li, G.; Chen, K. Iron-Nitrogen-Carbon Species Boosting Fast Conversion Kinetics of Fe_{1-x}S@C Nanorods as High Rate Anodes for Lithium Ion Batteries. *Chem. Eng. J.* **2018**, *338*, 726–733.
- (50) Zhang, S. S. The Redox Mechanism of FeS₂ in Non-Aqueous Electrolytes for Lithium and Sodium Batteries. *J. Mater. Chem. A* **2015**, *3*, 7689–7694.
- (51) Kong, F.; Fan, X.; Kong, A.; Zhou, Z.; Zhang, X.; Shan, Y. Covalent Phenanthroline Framework Derived FeS@Fe₃C Composite Nanoparticles Embedding in N-S-Codoped Carbons as Highly Efficient Trifunctional Electrocatalysts. *Adv. Funct. Mater.* **2018**, *28*, 1803973.
- (52) Strickland, K.; Miner, E.; Jia, Q.; Tylus, U.; Ramaswamy, N.; Liang, W.; Sougrati, M.-T.; Jaouen, F.; Mukerjee, S. Highly Active Oxygen Reduction Non-Platinum Group Metal Electrocatalyst without Direct Metal–Nitrogen Coordination. *Nat. Commun.* **2015**, *6*, 7343.
- (53) Zhao, L.; Yu, X.; Yu, J.; Zhou, Y.; Ehrlich, S. N.; Hu, Y.-S.; Su, D.; Li, H.; Yang, X.-Q.; Chen, L. Remarkably Improved Electrode Performance of Bulk MnS by Forming a Solid Solution with FeS–Understanding the Li Storage Mechanism. *Adv. Funct. Mater.* **2014**, *24*, 5557–5566.
- (54) Kostov, S.; DenBoer, M.; Strauss, E.; Golodnitsky, D.; Greenbaum, S. G.; Peled, E. X-Ray Absorption Fine Structure Studies of FeS₂ Cathodes in Lithium Polymer Electrolyte Batteries. *J. Power Sources* **1999**, *81–82*, 709–714.
- (55) BOUKAMP, B. Nonlinear Least Squares Fit Procedure for Analysis of Impedance Data of Electrochemical Systems. *Solid State Ionics* **1986**, *20*, 31–44.
- (56) Nobili, F.; Dsoke, S.; Mancini, M.; Tossici, R.; Marassi, R. Electrochemical Investigation of Polarization Phenomena and Intercalation Kinetics of Oxidized Graphite Electrodes Coated with Evaporated Metal Layers. *J. Power Sources* **2008**, *180*, 845–851.
- (57) Xiang, J. Y.; Wang, X. L.; Xia, X. H.; Zhong, J.; Tu, J. P. Fabrication of Highly Ordered Porous Nickel Phosphide Film and Its Electrochemical Performances toward Lithium Storage. *J. Alloys Compd.* **2011**, *509*, 157–160.
- (58) Carbonari, G.; Maroni, F.; Pasqualini, M.; Tossici, R.; Nobili, F. Preparation and Electrochemical Characterization of High-Stability MnO Anodes for Li-Ion Batteries. *Electrochim. Acta* **2017**, *247*, 392–399.
- (59) Maroni, F.; Gabrielli, S.; Palmieri, A.; Marcantoni, E.; Croce, F.; Nobili, F. High Cycling Stability of Anodes for Lithium-Ion Batteries Based on Fe₃O₄ Nanoparticles and Poly(Acrylic Acid) Binder. *J. Power Sources* **2016**, *332*, 79–87.
- (60) An, S. J.; Li, J.; Daniel, C.; Mohanty, D.; Nagpure, S.; Wood, D. L. The State of Understanding of the Lithium-Ion-Battery Graphite Solid Electrolyte Interphase (SEI) and Its Relationship to Formation Cycling. *Carbon* **2016**, *105*, 52–76.
- (61) Rezvani, S. J.; Nobili, F.; Gunnella, R.; Ali, M.; Tossici, R.; Passerini, S.; Di Cicco, A. SEI Dynamics in Metal Oxide Conversion Electrodes of Li-Ion Batteries. *J. Phys. Chem. C* **2017**, *121*, 26379–26388.
- (62) Rezvani, S. J.; Gunnella, R.; Witkowska, A.; Mueller, F.; Pasqualini, M.; Nobili, F.; Passerini, S.; Cicco, A. D. Is the Solid Electrolyte Interphase an Extra-Charge Reservoir in Li-Ion Batteries? *ACS Appl. Mater. Interfaces* **2017**, *9*, 4570–4576.
- (63) Liao, F.; Światowska, J.; Maurice, V.; Seyeux, A.; Klein, L. H.; Zanna, S.; Marcus, P. Electrochemical Lithiation and Passivation Mechanisms of Iron Monosulfide Thin Film as Negative Electrode Material for Lithium-Ion Batteries Studied by Surface Analytical Techniques. *Appl. Surf. Sci.* **2013**, *283*, 888–899.
- (64) Liao, F.; Światowska, J.; Maurice, V.; Seyeux, A.; Klein, L. H.; Zanna, S.; Marcus, P. The Influence of the Electrolyte on Chemical and Morphological Modifications of an Iron Sulfide Thin Film Negative Electrode. *Phys. Chem. Chem. Phys.* **2015**, *17*, 619–629.
- (65) Willmott, P. R.; Meister, D.; Leake, S. J.; Lange, M.; Bergamaschi, A.; Böge, M.; Calvi, M.; Cancellieri, C.; Casati, N.; Cervellino, A.; Chen, Q.; David, C.; Flechsig, U.; Gozzo, F.; Henrich, B.; Jäggi-Spielmann, S.; Jakob, B.; Kalichava, I.; Karvinen, P.; Krempasky, J.; Lüdeke, A.; Lüscher, R.; Maag, S.; Quitmann, C.; Reinle-Schmitt, M. L.; Schmidt, T.; Schmitt, B.; Streun, A.; Vartiainen, I.; Vitins, M.; Wang, X.; Wulschleger, R. The Materials Science Beamline Upgrade at the Swiss Light Source. *J. Synchrotron Radiat.* **2013**, *20*, 667–682.
- (66) Rodríguez-Carvajal, J. Recent Advances in Magnetic Structure Determination by Neutron Powder Diffraction. *Phys. B* **1993**, *192*, 55–69.
- (67) Parry, K. L.; Shard, A. G.; Short, R. D.; White, R. G.; Whittle, J. D.; Wright, A. ARXPS Characterisation of Plasma Polymerised Surface Chemical Gradients. *Surf. Interface Anal.* **2006**, *38*, 1497–1504.
- (68) Wang, D.; Bie, X.; Fu, Q.; Dixon, D.; Bramnik, N.; Hu, Y.-S.; Fauth, F.; Wei, Y.; Ehrenberg, H.; Chen, G.; Du, F. Sodium Vanadium Titanium Phosphate Electrode for Symmetric Sodium-Ion Batteries with High Power and Long Lifespan. *Nat. Commun.* **2017**, *8*, 15888.